A Spectral–Spatial Anomaly Target Detection Method Based on Fractional Fourier Transform and Saliency Weighted Collaborative Representation for Hyperspectral Images

Chunhui Zhao, Chuang Li , *Graduate Student Member, IEEE*, Shou Feng , Nan Su ,
and Wei Li , *Senior Member, IEEE*

Abstract—Anomaly target detection methods for hyperspectral images (HSI) often have the problems of potential anomalies and noise contamination when representing background. Therefore, a spectral–spatial hyperspectral anomaly detection method is proposed in this article, which is based on fractional Fourier transform (FrFT) and saliency weighted collaborative representation. First, hyperspectral pixels are projected to the fractional Fourier domain by the FrFT, which can enhance the capability of the detector to suppress the noise and make anomalies to be more distinctive. Then, a saliency weighted matrix is designed as the regularization matrix referring to context-aware saliency theory and combined with the FrFT-based collaborative representation detector. The saliency-weighted regularization matrix assigns different pixels with different weights by using both spectral and spatial information, which can reduce the influence of the potential anomalous pixels embedded in the background when applying collaborative representation theory. Finally, to further improve the performance of the proposed method, a spectral–spatial detection procedure is employed to calculate final anomaly scores by using both spectral information and spatial information. The proposed method is compared with nine state-of-the-art hyperspectral anomaly detection methods on six HSI datasets, including two synthetic HSI datasets and four real-world HSI datasets. Extensive experimental results illustrate that the proposed method's detection performance outperforms other nine well-known compared methods in terms of area under the receiver operating characteristic (ROC) curve values, visual detection characteristics, ROC curve, and separability.

Index Terms—Collaborative representation, context-aware saliency, fractional Fourier transform, hyperspectral anomaly target detection, spectral–spatial information.

Chunhui Zhao, Chuang Li, Shou Feng, and Nan Su are with the College of Information and Communication Engineering, Harbin Engineering University, Harbin 150001, China, and also with the Key Laboratory of Advanced Marine Communication and Information Technology, Ministry of Industry and Information Technology, Harbin Engineering University, Harbin 150001, China (e-mail: zhaochunhui1965@163.com; lichuang2017@hrbeu.edu.cn; fengshou1988@163.com; sunan08@hrbeu.edu.cn).

Wei Li is with the School of Information and Electronics, Beijing Institute of Technology, 100081 Beijing, China (e-mail: liwei089@ieee.org).

I. Introduction

IN RECENT years, hyperspectral remote sensing has attracted much attention on distinguishing different land surface materials. Hyperspectral image (HSI) is a 3-D data cube that contains rich spectral and spatial information simultaneously [1]. The spectral resolution of an HSI is no more than 10 nm, and the spectral range is from visible to even far-infrared spectrum. Therefore, an HSI usually has hundreds of spectral channels and can provide continuous spectral curves of the materials. Compared with traditional visible or multispectral remote sensing data, hyperspectral data contain richer spectral information, which are more suitable for many remote sensing applications, such as classification, target detection, and anomaly detection [2], [3].

Hyperspectral anomaly detection can be seen as a special type of target detection, where there is no prior information for the target object. Therefore, a target is called as an anomaly in the anomaly detection task. For the pixel under test (PUT) in an HSI, it is classified as an abnormal pixel or a background pixel by a hyperspectral anomaly detection method. As there is no requirement for any prior information [4], hyperspectral anomaly detection is viewed as an unsupervised binary classification problem [5]. As there is not enough information in practical applications, hyperspectral anomaly detection has been successfully applied in many important areas and scenarios [6], such as environmental scenes monitoring, mineral exploration, and military investigation [7].

In general, anomalies usually occur with low probabilities in an HSI and their spectral curves are significantly different with those of the background pixels [8]. To detect anomalies in HSIs correctly, many kinds of hyperspectral anomaly detection methods have been designed and proposed in the past decades. The well-known Reed–Xiaoli (RX) method is the most typical anomaly detection algorithm for HSIs in this field [9]. The RX method uses Mahalanobis distance to calculate the difference between the PUT and the background pixels. When the whole HSI is directly used for estimating the distribution of the background, the RX method is called as the global version of RX (GRX) [10]. And if a local sliding window is adopted to estimate the reference background, it is called as the local RX (LRX) [11]. Although

the RX method is used as a benchmark method for hyperspectral anomaly detection, its false-alarm rate (FAR) is usually high and its detection performance is not satisfactory. The main reason is that the RX method assumes that the distribution of the background is the multivariate normal Gaussian distribution [12], but the Gaussian distribution is too simple to model complex characteristics of the real HSIs accurately [13]. Besides, the problem that some anomalies and noise may contaminate the background can also reduce its detection performance [14].

In order to reduce the influences of the problems mentioned above, many revisions of the RX method have been proposed to get a high detection performance. For example, the weighted-RXD (WRX) method aimed to reduce the influence of anomalies on the covariance matrix when estimating background statistics [15]. The blocked adaptive computationally efficient outlier nominator (BACON) method was proposed in a paper by Billor *et al.* [16], which updates the background information based on an iteration strategy to solve the background contamination problem [17]. By taking advantage of nonlinear kernel function, the kernel-RX (KRX) is proposed to map the original data to a high-dimensional space, which can distinguish anomalies from the background pixels more easily in that feature space [18]. Furthermore, a modified KRX method was proposed in apaper by Khazai and Mojaradi [19] to improve the calculation efficiency of the traditional KRX. Du and Zhang [20] proposed the random-selection-based anomaly detector method, which adopted a sample random selection process to get a purified background set by picking out some representative pixels iteratively. The cluster-based anomaly detector, proposed by Carlotto [21], uses the k-means clustering method to segment the whole HSI and get a purer background. In order to suppress the noise in the background, the principal component analysis (PCA) technique is employed as a preprocessing procedure before using the RX method [22].

However, although these methods show their ability to improve the performance of RX, the basic distribution assumption for the background is not changed. Generally speaking, this assumption is not in line with the fact that the background distribution is very complicated in real-world HSIs and cannot be simply described as the Gaussian distribution [23]. To avoid estimating the statistical distribution of the background, other anomaly detection methods have been successfully proposed for real-world HSIs. As sparse representation (SR) theory has been successfully applied to image processing applications, some anomaly detection methods based on SR have been proposed for HSIs. For instance, a sparse representation hyperspectral anomaly detector was proposed by Chen *et al.* [24]. This method is based on the assumption that a background pixel can be well represented by only a few atoms from a sparse dictionary. Zhang *et al.* [25] proposed a hyperspectral anomaly detection method by using the low-rank and sparse matrix decomposition technique. This method decomposes the HSI data matrix into three parts: a low-rank matrix, a sparse matrix, and a noise matrix, which can provide more comprehensive information about the background pixels and anomalies. The SR-based methods have the advantage that there is no need to set up an assumption for the statistical data distribution of the HSI

dataset [26]. To preserve the local geometrical structure and spatial information in the HSI, an anomaly detection method based on graph and total variation regularized low-rank representation (GTVLRR) is proposed [27]. But they also have a drawback that it is hard to select a suitable sparsity level as there is no prior information that can be used. Li and Du [28] proposed a collaborative representation-based anomaly detector (CRD) for HSIs. Compared to SR-based methods, the CRD method utilizes the constraint of l_2 norm minimization, and the pixel under test is represented by all background pixels, which is easier to implement. Su *et al.* [29] combined PCA with CRD to propose a new anomaly detection method, in which the usage of PCA is to extract the main information of the background and to remove anomalies and noise in the background.

There are still other hyperspectral anomaly detection methods proposed in the related literature, such as the supporting vector data description (SVDD) method [30]. In SVDD, a minimum hypersphere boundary is calculated according to the HSI data, and pixels beyond the boundary are decided as anomalies. The anomaly detection methods mentioned above are most only based on spectral signatures. As an HSI is viewed as a 3D data cube [31], it not only contains abundant spectral information, but also contains the spatial information. By taking advantage of these characteristics, anomaly detection methods have been designed by making use of both spatial information and spectral information [32]. For example, local sparsity divergence (LSD) detector proposed in paper [33] is a spectral–spatial anomaly detection method. The assumption of the LSD method is that an anomaly pixel cannot be represented by only a few background pixels selected from its spectral neighbors or its spatial neighbors simultaneously.

Although these hyperspectral anomaly detection methods have proven their effectiveness in related studies, some other important issues can also affect the detection performance of these methods. The first problem is that the background information is usually contaminated by the anomalies or noise [34]. As real-world HSIs commonly contain various materials with different spectral properties, noise is inevitably included, which can deteriorate the detection performance when modeling the background. Besides, when using the whole HSI to extract background pixels, anomalies may interfere the estimation of the background. To reduce these effects, a sliding rectangular window or dual window is adopted to select reliable background pixels. However, some anomalies can also be selected as background pixels, which will reduce the detection performance of the method. The second problem is how to make use of the rich spatial information of HSIs, as taking advantage of both spatial information and spectral information can improve the performance of an anomaly detection method [35].

In order to solve these two issues, a novel spectral–spatial anomaly target detection method based on fractional Fourier transform (FrFT) , context-aware saliency, and collaborative representation theory (SSFSCRD) is proposed for HSIs in this article. First, an FrFT-based CRD is designed and the original HSI data are projected to the FrFT domain. By taking advantage of the fractional Fourier transform, the noise suppression and discrimination capability of the detector between anomalies and

background can be enhanced [36]. Then, a saliency-weighted matrix is proposed for the FrFT-based CRD as the regularization matrix. Inspired by the visual saliency theory, the similarity of two pixels are not only depended on their spectral information, but also related with their spatial position information. The new saliency-weighted regularization matrix used in the collaborative representation theory is designed based on this idea, which can reduce the effect of the abnormal pixel information mixed in the background when applying collaborative representation theory. Hence, the background can be represented more accurately and precisely. Finally, the SSFSCRD method also contains a spectral–spatial detection procedure to get the final results, which can use both spectral information and spatial information to enhance the anomaly detection performance. All of these three parts can ensure that the performance of the proposed SSFSCRD method is better when compared with other state-of-the-art detection methods. Extensive experiments on two synthetic HSI datasets and four real-world HSI datasets are carried out to show the effectiveness and performance of the proposed method. When compared with nine state-of-the-art hyperspectral anomaly detectors, the detection performance of the proposed method outperforms other compared detectors in terms of area under the receiver operating characteristic (ROC) curve (AUC) values, visual detection characteristics, ROC curves, and separability. The main contributions of the proposed SSFSCRD method are as follows.

1) The FrFT is employed to design the FrFT-based CRD in the proposed method. By taking advantage of the FrFT, not only the influence of noise on the detection accuracy can be reduced, but also the discrimination between the background and anomalies can be improved to some extent.

2) Learning from the relevant principles of visual saliency theory, a saliency-weighted regularization matrix is proposed according to context-aware saliency and combined with the FrFT-based CRD. The new regularization matrix uses both spectral and spatial information to set the weights for the background pixels. By adjusting the weights of each pixel in the selected background, the interference of potential anomalies to the detection accuracy is reduced.

3) A spectral–spatial detection procedure is designed and integrated in the proposed method to get the final detection results. Through the comprehensive utilization of both spectral information and spatial information, the detection performance of the proposed SSFSCRD method is further improved.

The remainder of this article is structured as follows. Section II introduces the details of the proposed method. The experimental datasets, settings and results of the proposed method and other methods are given in Section III. Section IV discusses and analyzes the parameters of the proposed method. Finally, the conclusion of this article is outlined in Section V.

II. THE PROPOSED METHOD

The proposed SSFSCRD method mainly includes three parts. In the beginning, the HSI data is projected to fractional Fourier

domain by using FrFT. Then, a saliency-weighted FrFTCRD is used to get the preliminary detection result of the HSI. Finally, a spectral-spatial detection procedure is applied to get the final anomaly detection result. The framework of the proposed method is shown in Fig. 1.

A. Collaborative Representation-Based Detector

In order to explain the CRD method clearly, some mathematical definitions and notations are given first. Let $\mathbf{X} = \{\mathbf{x}^i\}_{i=1}^{M \times N} \in R^{L \times M \times N}$ be a 3D HSI data cube, where L is the number of spectral bands. $\mathbf{x}^i$ is the ith spectral vector which can be written as $\mathbf{x}^i = (x_1^i, x_2^i, \dots, x_L^i)^T$. Denote the total number of pixels in $\mathbf{X}$ as D, where $D = M \times N$, and $\mathbf{X}$ can be rewritten as a 2-D matrix $\mathbf{X} = \{\mathbf{x}^i\}_{i=1}^{D} \in R^{L \times D}$.

The basic idea of collaborative representation theory is that a pixel belonging to the background of an HSI can be represented by its spatial neighborhoods, while an anomaly cannot. The spatial neighborhoods of a PUT form its background set, which can be considered as a reconstruction dictionary used in the SR theory. A sliding dual-window is adopted to select the spatial neighborhoods of a PUT, and the pixels between the inner window and the outer window are used as the background set, or as atoms of the dictionary. For an under test pixel $\mathbf{y}$, let w_{in} be the size of the inner window and w_{out} be the size of the outer window, and the pixel number of the background set can be calculated as $s = w_{\text{out}} \times w_{\text{out}} - w_{\text{in}} \times w_{\text{in}}$. Therefore, the background set can be denoted as a matrix $\mathbf{X}_s = \{\mathbf{x}^j\}_{j=1}^{s}$, where $\mathbf{x}^j$ represents a pixel between the outer and inner windows.

For an under-test pixel $\mathbf{y}$, its collaborative representation weight vector α is minimized by the following formulation:

$$\arg \min_{\alpha} ||\mathbf{y} - \mathbf{X}_s \alpha|| + \lambda ||\alpha||_2^2 \qquad (1)$$

where λ is a Lagrange multiplier.

(1) is equivalent to the following formulation:

$$\arg \min_{\alpha} [\alpha^T (\mathbf{X}_s^T \mathbf{X}_s + \lambda \mathbf{I}) \alpha - 2\alpha^T \mathbf{X}_s^T \mathbf{y}]. \qquad (2)$$

The weight vector α can be calculated by taking derivative with regard to α of (2) and setting the resultant equation to zero, which can be written as the following equation:

$$\alpha = (\mathbf{X}_s^T \mathbf{X}_s + \lambda \mathbf{I})^{-1} \mathbf{X}_s^T \mathbf{y}. \qquad (3)$$

Considering the spectral similarity among the under-test pixel and its each surrounding pixels in the matrix is different, so a regularization matrix $\Gamma_{\mathbf{y}}$ is introduced as

$$\Gamma_{\mathbf{y}} = \begin{bmatrix} ||\mathbf{y} - \mathbf{x}^1||_2 & \cdots & 0 \\ \vdots & \ddots & \vdots \\ 0 & \cdots & ||\mathbf{y} - \mathbf{x}^s||_2 \end{bmatrix} \qquad (4)$$

where $\mathbf{x}^1, \mathbf{x}^2, \dots, \mathbf{x}^s$ are the elements of the set $\mathbf{X}_s$.

Adding the regulation $\Gamma_{\mathbf{y}}$ to (1), the optimization function is modified as

$$\arg \min_{\alpha} ||\mathbf{y} - \mathbf{X}_s \alpha|| + \lambda ||\Gamma_{\mathbf{y}} \alpha||_2^2. \qquad (5)$$

Accordingly, the final result of α can be written as

$$\alpha = (\mathbf{X}_s^T \mathbf{X}_s + \lambda \Gamma_{\mathbf{y}}^T \Gamma_{\mathbf{y}})^{-1} \mathbf{X}_s^T \mathbf{y}. \qquad (6)$$
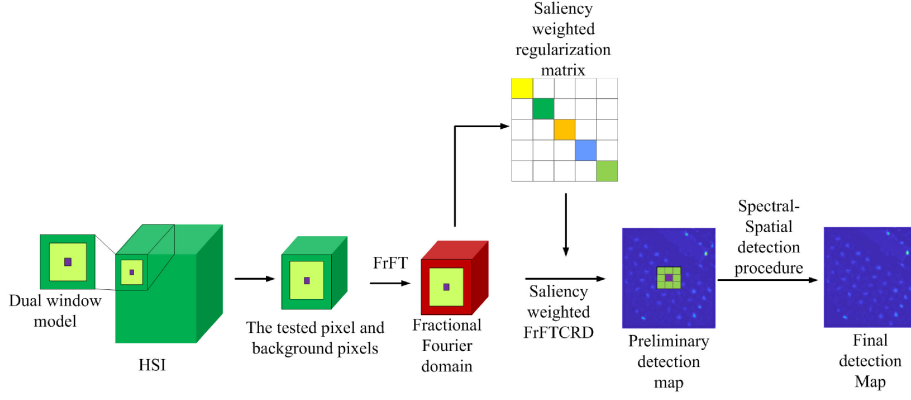
Fig. 1. Framework of the proposed method.

With the matrix $\mathbf{X}_s$ and the weight vector α, the PUT $\mathbf{y}$ can be reconstructed as

$$\hat{\mathbf{y}} = \mathbf{X}_s\alpha \qquad (7)$$

where $\hat{\mathbf{y}}$ is the reconstructed pixel of $\mathbf{y}$.

The residual error between $\mathbf{y}$ and its reconstructed pixel $\hat{\mathbf{y}}$ can be calculated as

$$r_1 = ||\mathbf{y} - \hat{\mathbf{y}}||_2 = ||\mathbf{y} - \mathbf{X}_s\alpha||_2. \qquad (8)$$

If r_1 is larger than a given threshold σ, then the PUT is determined as an anomaly.

B. Fractional Fourier Transform-Based CRD

The FrFT is an extension version of the traditional Fourier transform (FT) [37]. By using FrFT, HSI pixels can be transferred into the fractional Fourier domain, and the features obtained in this domain contains the information of both original spectral domain and frequency Fourier domain. Projecting HSI data to the fractional Fourier domain can not only suppress the noise in the background, but also increase the discrimination of anomalies. By taking advantage of these merits mentioned above, FrFT is combined with CRD (FrFTCRD) to process the HSI data in the proposed method.

Let $\mathbf{x}^i = (x_1^i, x_2^i, \ldots, x_L^i)^T$ be a pixel in $\mathbf{X} = \{\mathbf{x}^i\}_{i=1}^{M \times N}$, and its representation through FrFT is denoted as $\varphi(\mathbf{x}^i)$, where $\varphi(\mathbf{x}^i) = (x_p^i(1), (x_p^i(2), \ldots, x_p^i(L))^T$ can be calculated by the following equation:

$$x_p^i(u) = \frac{1}{L}\sum_{f=1}^{L} x_f^i K_p(f, u) \qquad (9)$$

in which u and f are indices and p is the fractional order of FrFT. In (9), $K_p(f, u)$ is defined as

$$K_p(f, u) = \begin{cases} A_\phi exp[j\pi(f^2\cot\phi - 2fucsc\phi + u^2\cot\phi)] \\ , \phi \neq n\pi \\ \delta(f - u), \phi = 2n\pi \\ \delta(f + u), \phi = (2n \pm 1)\pi \end{cases} \qquad (10)$$

where the rotation angle ϕ is related to p as $\phi = \frac{p\pi}{2}$ [38], and A_ϕ can be figured out by

$$A_\phi = \frac{exp[-j\pi sgn(\sin\phi)/4 + j\phi/2]}{|\sin\phi|^{\frac{1}{2}}}. \qquad (11)$$

To implement FrFT into CRD, the new optimization problem can be written as

$$\arg\min_{\alpha} ||\tilde{\varphi}(\mathbf{y}) - \tilde{\varphi}(\mathbf{X}_s)\alpha|| + \lambda||\Gamma_{\tilde{\varphi}(\mathbf{y})}\alpha||_2^2 \qquad (12)$$

where $\tilde{\varphi}(\mathbf{y})$ is the amplitude of $\varphi(\mathbf{y})$, $\tilde{\varphi}(\mathbf{X}_s) = \{\tilde{\varphi}(\mathbf{x}^j)\}_{j=1}^s$, and $\Gamma_{\tilde{\varphi}(\mathbf{y})}$ is defined as

$$\Gamma_{\tilde{\varphi}(\mathbf{y})} = \begin{bmatrix} ||\tilde{\varphi}(\mathbf{y}) - \tilde{\varphi}(\mathbf{x}^1)||_2 & \cdots & 0 \\ \vdots & \ddots & \vdots \\ 0 & \cdots & ||\tilde{\varphi}(\mathbf{y}) - \tilde{\varphi}(\mathbf{x}^s)||_2 \end{bmatrix}. \qquad (13)$$

The weight vector α can be calculated by the following equation:

$$\alpha = (\tilde{\varphi}^T(\mathbf{X}_s)\tilde{\varphi}(\mathbf{X}_s) + \lambda\Gamma_{\tilde{\varphi}(\mathbf{y})}^T\Gamma_{\tilde{\varphi}(\mathbf{y})})^{-1}\tilde{\varphi}^T(\mathbf{X}_s)\tilde{\varphi}(\mathbf{y}). \qquad (14)$$

Then, the anomaly score is represented by

$$r_1 = ||\tilde{\varphi}(\mathbf{y}) - \tilde{\varphi}(\mathbf{X}_s)\alpha||_2. \qquad (15)$$

C. Saliency-Weighted FrFTCRD

The regularization matrix $\Gamma_{\mathbf{y}}$ used in the CRD can assign pixels in the background with different weights. These weights are only calculated based on the spectral information, which cannot well eliminate the influence of potential anomalies on the background. To solve this problem, a new regularization matrix is designed referring to the relevant principles of context-aware saliency. The new regularization matrix can use both spectral and spatial information to set the weights for the background pixels, which can further reduce the influence of potential anomalies. Combined with FrFT and CRD, a saliency-weighted FrFTCRD is proposed for hyperspectral anomaly detection.

Detecting the salient regions of an image is a challenging issue in the filed of computer vision. The context-aware saliency detection method was proposed by Goferman *et al.* [39], and its

basic idea is that salient regions are distinctive with respect to both their local and global surroundings [40]. From the psychological point of view, human visual attention mechanism follows four basic principles: local considerations, global considerations, visual organization rules, and some prior information.

According to these four principles, the context-aware saliency detection method defined a dissimilarity measure d between two patches p_i and p_j of an image as [41]

$$d(p_i, p_j) = \frac{d_{\text{color}}(p_i, p_j)}{1 + c \times d_{\text{position}}(p_i, p_j)} \tag{16}$$

where d_{color} is the euclidean distance between patches p_i and p_j in the color space, and d_{position} is the euclidean distance between the positions of patches p_i and p_j.

It is easy to find that the dissimilarity measure is proportional to the appearance difference and inversely proportional to the positional distance. Based on this idea of saliency, we proposed a hyperspectral dissimilarity measure to quantitatively represent the dissimilarity between the under-test pixel $\mathbf{y}$ and a pixel $\mathbf{x}^i$ in the background set $\mathbf{X}_s$. Let d_{position} be the relative positional distance between $\mathbf{y}$ and $\mathbf{x}^i$, the hyperspectral dissimilarity measure d_h can be defined as

$$d_h(\mathbf{y}, \mathbf{x}^i) = \frac{||\mathbf{y} - \mathbf{x}^i||_2}{d_{\text{position}}(\mathbf{y}, \mathbf{x}^i)}. \tag{17}$$

By taking advantage of the hyperspectral dissimilarity measure d_h, a new saliency-weighted regularization matrix $\Gamma_{\mathbf{y}}^S$ is defined as

$$\Gamma_{\mathbf{y}}^S = \begin{bmatrix} \frac{||\mathbf{y} - \mathbf{x}^1||_2}{d_{\text{position}}(\mathbf{y}, \mathbf{x}^1)} & \cdots & 0 \\ \vdots & \ddots & \vdots \\ 0 & \cdots & \frac{||\mathbf{y} - \mathbf{x}^s||_2}{d_{\text{position}}(\mathbf{y}, \mathbf{x}^s)} \end{bmatrix}. \tag{18}$$

This new saliency-weighted regularization matrix is combined with FrFT and CRD to form a saliency-weighted FrFTCRD method. The optimization function of the saliency-weighted FrFTCRD method can be written as

$$\arg\min_{\alpha} ||\tilde{\varphi}(\mathbf{y}) - \tilde{\varphi}(\mathbf{X}_s)\alpha|| + \lambda ||\Gamma_{\tilde{\varphi}(\mathbf{y})}^S \alpha||_2^2 \tag{19}$$

where $\Gamma_{\tilde{\varphi}(\mathbf{y})}^S$ is defined as

$$\Gamma_{\tilde{\varphi}(\mathbf{y})}^S = \begin{bmatrix} \frac{||\tilde{\varphi}(\mathbf{y}) - \tilde{\varphi}(\mathbf{x}^1)||_2}{d_{\text{position}}(\tilde{\varphi}(\mathbf{y}), \tilde{\varphi}(\mathbf{x}^1))} & \cdots & 0 \\ \vdots & \ddots & \vdots \\ 0 & \cdots & \frac{||\tilde{\varphi}(\mathbf{y}) - \tilde{\varphi}(\mathbf{x}^s)||_2}{d_{\text{position}}(\tilde{\varphi}(\mathbf{y}), \tilde{\varphi}(\mathbf{x}^s))} \end{bmatrix}. \tag{20}$$

Accordingly, the weight vector α can be calculated by the following equation:

$$\alpha = (\tilde{\varphi}^T(\mathbf{X}_s)\tilde{\varphi}(\mathbf{X}_s) + \lambda(\Gamma_{\tilde{\varphi}(\mathbf{y})}^S)^T \Gamma_{\tilde{\varphi}(\mathbf{y})}^S)^{-1} \tilde{\varphi}^T(\mathbf{X}_s)\tilde{\varphi}(\mathbf{y}). \tag{21}$$

Then, the anomaly score of the saliency-weighted FrFTCRD method can be figured out by

$$r_1 = ||\tilde{\varphi}(\mathbf{y}) - \tilde{\varphi}(\mathbf{X}_s)\alpha||_2. \tag{22}$$

Algorithm 1: The Framework of SSFSCRD Algorithm.

Input:
  $\mathbf{X}$: Three-dimensional hyperspectral image; w_{in}: the inner window size; w_{out}: the outer window size; p: the fractional order; the regularization parameter λ; the weighting coefficient β.

Output:
  Anomaly detection map.

  1: **forall** Pixels **do**
  2: For each under test pixel $\mathbf{y}$, obtain its background set $\mathbf{X}_s$
  3:      Project $\mathbf{y}$ and $\mathbf{X}_s$ to the fractional Fourier domain by using (9)
  4:      Calculate the new saliency weighted regularization matrix by using (18)
  5:      Calculate the weight vector α by using (21)
  6:      Calculate the anomaly score according to (22)
  7: **endfor**
  8: **for all** pixels **do**
  9:      For each under test pixel $\mathbf{y}$, calculate its final anomaly score according to (23)
  10: **endfor**

D. Spectral–Spatial Detection Procedure

Many studies have proved that taking advantage of spatial information can improve the performance of a hyperspectral anomaly detection method. Although the saliency-weighted FrFTCRD has comprehensively utilized both spectral and spatial information, a spectral–spatial detection procedure is proposed in this section to make further use of spatial information.

According to the characteristics of hyperspectral remote sensing, a pixel and its surrounding pixels in an HSI usually reflect the same or similar ground objects. Therefore, when these pixels are represented by CRD, their residual errors should be approximately the same [42]. Based on this assumption, the spatial information can be incorporated for HSI anomaly detection by considering the relative position of a PUT and its neighbors. The closer relative position between the PUT and a neighbor pixel means their residual errors are more similar.

In this spectral–spatial detection procedure, the anomaly score of an under-test pixel is assigned as the weighted value of its residual error and the weighted average value of its adjacent pixels' residual errors. For a PUT $\mathbf{y}$, this strategy can be written as the following formula:

$$r^{\mathbf{y}} = \beta r_1^{\mathbf{y}} + (1 - \beta) \sum_{i \in \psi} \frac{\frac{1}{e^{d_{position}((\mathbf{y}),(\mathbf{x}^i)) + |r_1^{\mathbf{y}} - r_1^i|}}}{\sum_{j \in \psi} \frac{1}{e^{d_{position}((\mathbf{y}),(\mathbf{x}^j)) + |r_1^{\mathbf{y}} - r_1^j|}}} r_1^i \tag{23}$$

where $r^{\mathbf{y}}$ is the final anomaly score of the PUT $\mathbf{y}$, ψ is the set of its adjacent pixels, β is the weighting coefficient, and $r_1^{\mathbf{y}}$ and r_1^i are the residual errors calculated by formula (22).

This spectral–spatial detection procedure uses relative positional information and anomaly scores of PUT and its adjacent
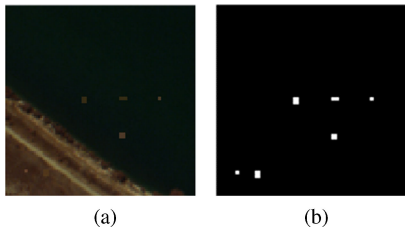
Fig. 2. First synthetic dataset. (a) False-color image. (b) Ground truth.

pixels calculate anomaly score of the PUT, and can reduce the influence of noise contamination in the background. Furthermore, this strategy is independent of the detection process, with less calculation and easy to implement. The main steps of SSFSCRD are summarized in Algorithm 1.

III. EXPERIMENTAL RESULTS

In this section, a number of experiments are conducted to show the performance and effectiveness of the proposed method from different perspectives. The details of two synthetic HSI datasets and four real-world HSI datasets used in the experiments are introduced first. Next, the relevant settings of the experiment and the selected evaluation criteria are given. Finally, the experimental results of the proposed method and the compared methods are analyzed.

A. Experimental Datasets

There are totally six hyperspectral datasets selected for conducting experiments, which include two synthetic HSI datasets and four real-world HSI datasets. These HSI datasets were captured by two different sensors over different kinds of scenes, and their spatial resolution and spectral resolution are also different. With the help of these different datasets, the performance and effect of the proposed method can be tested more comprehensively. The details of these HSI datasets are described in the following part.

1) Synthetic HSI Datasets: The first one synthetic HSI dataset (hereinafter referred to as S1) was collected over Pavia, Northern Italy, by the Reflective Optics System Imaging Spectrometer (ROSIS) sensor [43]. Its size is 105×100 pixels with 102 spectral bands. The spatial resolution is 1.3 m, and the spectral resolution is 4 nm. Six anomalies were scattered in the background with white noise to get the synthetic HSI dataset. The sizes of these anomalies are 4×3, 4×3, 2×2, 2×2, 3×3, and 2×4, respectively. The false-color image of the first synthetic data is shown in Fig. 2(a), and positions of six anomalies are shown in Fig. 2(b).

The second synthetic HSI dataset (hereinafter referred to as S2) was also collected by the ROSIS sensor, over Pavia University, Northern Italy. So its spatial resolution and spectral resolution are the same with those of the S1 dataset. The S2 dataset consists 300×200 pixels and the number of its spectral bands is 103. The synthetic anomalies are embedded into the background by using the following equation [44]:

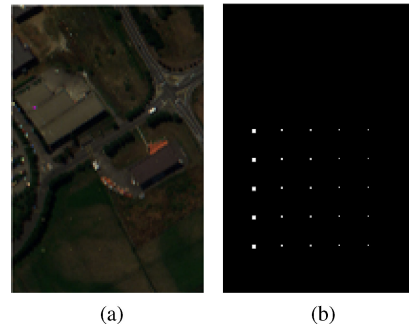$$S = B \times (1 - p) + T \times p \tag{24}$$

Fig. 3. Second synthetic dataset. (a) False color image. (b) Ground truth.
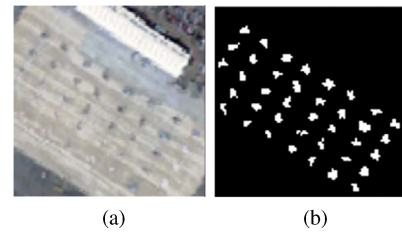

Fig. 4. First real dataset. (a) False color image. (b) Ground truth.

where T is the pure anomalous pixel, B is the selected background pixel, and the p is the mixture percentage of the anomalies. The false-color image of the second synthetic HSI data is shown in Fig. 3(a), and the ground truth is given in Fig. 3(b). It can be found that there are 25 anomalies in total, and the sizes of these anomaly targets are 2×1, 1×2, 2×2, and 3×2, respectively.

2) Real HSI Datasets: Four different real HSI datasets which are widely used in many related studies are selected for the experiment. These HSIs were captured over different locations by two different imaging spectrometer sensors. Their scenes, the number of spectral bands, spatial and spectral resolution, and anomalies selected to be detected are also different. Therefore, these four real HSI datasets are very suitable for testing the comprehensive detection performance of the proposed method under different scenes and circumstances.

The first real HSI dataset (hereinafter referred to as R1) is collected by airborne visible infrared imaging spectrometer (AVIRIS). It is a part of the real HSI of the San Diego International Airport, USA [45]. The selected image contains 38 anomalies, and its size is 100×100 pixels with 126 spectral bands. The spatial resolution is 3.5 m, and the spectral resolution is 10 nm. The false-color image of this dataset is shown in Fig. 4(a). The actual distribution of 38 anomalies is shown in Fig. 4(b).

The second real HSI dataset (hereinafter referred to as R2) is also collected by the AVIRIS sensor [46]. It is a HSI of an airport in Los Angeles, USA [47]. The spatial resolution is 7.1 m, and its spectral resolution is the same as R1's. The image has 224 spectral channels in wavelengths ranging from 400 to 2500 nm. After removing the bands severely affected by moisture and the low-signal-to-noise (SNR) bands, there are 204 spectral bands remained. The size of the R2 HSI data is 100×100 pixels, and
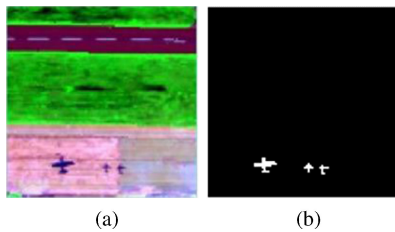
Fig. 5.   Second real dataset. (a) False-color image. (b) Ground truth.
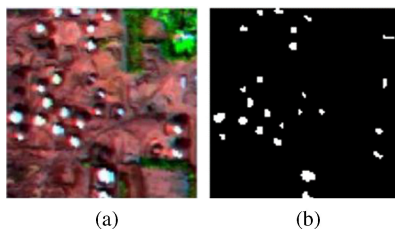

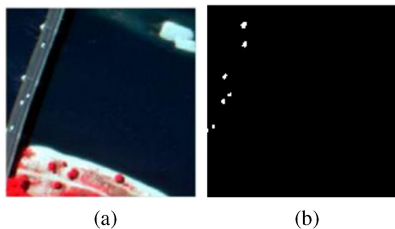Fig. 6.   Third real dataset. (a) False-color image. (b) Ground truth.

Fig. 7.   Fourth real dataset. (a) False-color image. (b) Ground truth.

there are three anomalies in it [6]. The false color image of the R2 dataset is shown in Fig. 5(a), and its corresponding ground truth is shown in Fig. 5(b).

The third HSI dataset (hereinafter referred to as R3) is an urban scene of Texas coast, USA [48]. It is also captured by the AVIRIS sensor, and its spatial resolution is 17.2 m. There are 207 spectral bands in this image, whose wavelengths range from 400 to 2500 nm. The image size of the HSI data is 100×100 pixels, and are chosen as anomalies. The false color image of the R3 HSI dataset is shown in Fig. 6(a), and its corresponding ground truth is shown in Fig. 6(b).

The fourth real HSI dataset (hereinafter referred to as R4) was collected by the ROSIS sensor over the Pavia city in Northern Italy [49]. The spatial resolution is 1.3 m, and the spectral resolution is 4 nm. The R4 image's size is 150×150 pixels, and it has 102 spectral bands in wavelengths ranging from 430 to 860 nm. The vehicles in the R4 HSI dataset are selected as anomalies [50]. The false-color image of the R4 HSI dataset and the image of its ground truth are shown in Fig. 7(a) and (b).

B. Evaluation Criteria and Experimental Settings

In this part, the evaluation criterion, compared methods, and parameter settings related to experiments are introduced as follows.

1) Evaluation Criteria: In order to accurately evaluate and analyze the performance detection efficiency of a hyperspectral

anomaly detector qualitatively and quantitatively, the ROC curve and the AUC value are adopted as evaluation criteria [6].

The ROC curve is the most commonly used evaluation criterion used in the area of hyperspectral anomaly detection [51]. It shows the relationship between the FAR and the true positive rate (TPR) under different threshold. The FAR and TPR can be figured out as follows, respectively.

$$FAR = \frac{FP}{FP + TN} \qquad (25)$$

$$TPR = \frac{TP}{TP + FN} \qquad (26)$$

where TP is the number of anomalies that were also predicted as anomalies, TN is the number of background pixels that were predicted correctly, FN is the number of anomalies but wrongly predicted as background pixels, and FP is the number of background pixels but wrongly predicted as anomalies [52].

For a set of methods, a method that has a higher TPR value when compared with others under the same FAR can be considered to have better performance. The AUC value is used to show the average performance of a method, which can be calculated by carrying out the integral operator for ROC curve [53]. It should be noted that the larger the value of AUC is, the better a detector performs.

2) Compared Methods: To verify the performance of the proposed method, nine hyperspectral anomaly detection methods which are commonly used as compared methods in many studies are selected for complete comparison. The compared methods include the GRX method, LRX method, KRX method, CRD method, KCRD method, PCA-RX method, FrFE+RX method, GTVLRR method, and LSD method.

These methods are selected as competitors by considering the diversity and popularity comprehensively. Specially, GRX and LRX are two versions of the benchmark Reed–Xiaoli method which are based on the statistical distribution hypothesis of the background. CRD is the classical CRD. KRX and KCRD are the RX and CRD methods combined with the kernel function theory.

As the proposed method used FrFT and context-aware saliency to suppress noise, reduce the effect of the anomalies and enhance the discrimination between background pixels and anomalies, some related detectors are chosen. FrFE+RX is the combination of FrFT and RX proposed by Tao *et al.* [36]. In addition, as the proposed method takes advantage of both spectral and spatial information, a spectral–spatial detector, the LSD detector, is also added to the set of compared methods. LSD is based on the assumption that an abnormal pixel cannot be represented by very few background samples from the local surrounding both in the spectral and spatial domains. GTVLRR is the representative of the low-rank and sparse-based methods, which incorporates the local geometrical structure and spatial information of an HSI.

In summary, it can be found that different types of anomaly detectors are chosen as competitors. Therefore, the choice of the comparison methods is suitable and reasonable, which can be used to show the performance of the proposed method effectively and accurately.

TABLE I
OPTIMAL PARAMETER SETTINGS FOR THE TESTED METHODS

Methods	Parameter	S1	S2	R1	R2	R3	R4
LRX	w_{in}	3	3	5	9	5	15
	w_{out}	5	5	7	13	11	17
KRX	w_{in}	3	3	9	5	3	15
	w_{out}	11	11	11	13	7	17
	σ	10^{-1}	10^4	1	10^{-6}	10^{-5}	1
CRD	w_{in}	9	7	9	19	11	3
	w_{out}	11	23	11	21	13	17
	λ	10^{-6}	10^{-6}	10^{-6}	10^{-6}	10^{-6}	10^{-6}
KCRD	w_{in}	5	17	7	19	7	3
	w_{out}	13	19	9	21	9	5
	λ	10^{-11}	10^{-6}	10^{-6}	10^{-6}	10^{-4}	10
	σ	10	10	10	10	10	10
PCA+RX	n	8	5	10	3	10	10
GTVLRR	λ	0.5	0.5	0.5	0.5	0.5	0.5
	β	0.2	0.2	0.2	0.2	0.2	0.2
	γ	0.1	0.005	0.05	0.01	0.01	0.005
LSD	w_{in}	5	5	7	9	3	11
	w_{out}	7	7	17	19	9	17
	n	8	1	9	5	2	1
SSFSCRD	w_{in}	9	7	9	5	11	5
	w_{out}	11	9	11	7	13	9
	p	0.8	0.7	0.3	1	0.3	0.3
	λ	10^2	10^4	10^{-5}	10^3	10^6	10^3
	β	1	1	0.5	0.2	0.2	0.1

3) Parameter Settings: All the programs and experiments are run by MATLAB 2017 on a workstation with core i7-7700, CPU@2.8 GHz and 16-GB RAM. The code for the proposed SSFSCRD method is available online.[1] The optimal parameter settings of these compared methods are given in Table I. LRX method has two parameters: inner window size w_{in} and outer window size w_{out}. KRX method has three parameters: inner window size w_{in}, outer window size w_{out}, and kernel parameter σ. CRD method has three parameters: inner window size w_{in}, outer window size w_{out}, and regularization parameter λ. KCRD method has four parameters: inner window size w_{in}, outer window size w_{out}, regularization parameter λ, and kernel parameter σ. PCA+RX method has just one parameter: optimal principal component n. GTVLRR method has three parameters: tradeoff parameters λ, β, and γ. LSD method has three parameters: inner window size w_{in}, outer window size w_{out}, and optimal principal component n. There are five critical parameters in the proposed method: inner window size w_{in}, outer window size w_{out}, fractional order p, Lagrange multiplier λ, and the weighting coefficient β. The details of corresponding parameter selection experiments and the effect of these parameters are conducted and analyzed in tSection IV.

C. Experimental Results and Analysis

In order to evaluate the performance of the proposed method comprehensively and convincingly, extensive experimental results are deeply discussed and analyzed in this part. Table II shows the AUC values of the respective methods on all synthetic and real HSI datasets, and the best value in each HSI dataset is highlighted in italics. The AUC values of the proposed method obtained in two synthetic HSI datasets and four real HSI datasets are 0.9856, 0.9494, 0.9761, 0.9935, 0.9957, and 0.9989, respectively. It can be clearly found that the proposed method is superior to all other compared methods on all six

[1][Online]. Available: https://github.com/lichuang0529/SSFSCRD

TABLE II
AUC SCORES OF THE GRX, LRX, KRX, CRD, KCRD, PCA+RX, FRFE+RX, GTVLRR, LSD, AND SSFSCRD METHODS ON SIX DATASETS

Methods	The synthetic datasets		The real datasets			
	S1	S2	R1	R2	R3	R4
GRX	0.6465	0.8082	0.6899	0.9742	0.9889	0.9516
LRX	0.6202	0.6521	0.7949	0.9273	0.9404	0.9084
KRX	0.8990	0.6769	0.7538	0.9785	0.8541	0.9138
CRD	0.9711	0.9281	0.9632	0.9840	0.9633	0.9737
KCRD	0.9389	0.9411	0.9503	0.9919	0.9832	0.9879
PCA+RX	0.9536	0.6650	0.7720	0.9801	0.9879	0.9498
FrFE+RX	0.7684	0.5897	0.7472	0.9742	0.9765	0.9505
GTVLRR	0.9092	0.8375	0.7882	0.9578	0.9082	0.9716
LSD	0.9655	0.8103	0.7520	0.9680	0.9955	0.9105
SSFSCRD	**0.9856**	**0.9494**	**0.9761**	**0.9935**	**0.9957**	**0.9989**

TABLE III
AUC SCORES OF THE GRX, LRX, KRX, CRD, KCRD, PCA+RX, FRFE+RX, GTVLRR, LSD, AND SSFSCRD METHODS ON SIX DATASETS WITH THE SAME DUAL WINDOW SIZES

Methods	The synthetic dataset		The real dataset			
	S1	S2	R1	R2	R3	R4
GRX	0.6465	0.8082	0.6899	0.9742	0.9889	0.9516
LRX	0.4798	0.5196	0.7791	0.8110	0.9094	0.9044
KRX	0.8781	0.6598	0.7413	0.9325	0.6561	0.8987
CRD	0.9679	0.8497	0.9617	0.8682	0.9632	0.9200
KCRD	0.9187	0.9237	0.9500	0.9672	0.9702	0.9772
PCA+RX	0.9151	0.6650	0.5590	0.9010	0.9829	0.9387
FrFE+RX	0.7684	0.5897	0.7472	0.9470	0.9765	0.9505
GTVLRR	0.7952	0.8375	0.7882	0.9578	0.9082	0.9716
LSD	0.9552	0.8103	0.7165	0.9533	0.9955	0.9105
SSFSCRD	**0.9856**	**0.9494**	**0.9761**	**0.9935**	**0.9957**	**0.9989**

datasets. Furthermore, as the spatial and spectral resolution of the experimental HSIs is different, it can be observed that the proposed method can provide a much more stable detection result and have a good performance on datasets with different spatial and spectral resolution. Results on these different datasets can show that the proposed SSFSCRD method is suitable for different kinds of datasets. Besides, AUC scores of SSFSCRD method and compared methods on six datasets with the same dual window sizes are shown in Table III. It can be declared that the AUC values of SSFSCRD method is also superior to all other compared methods on all six datasets with the same dual window sizes.

Figs. 8–13 illustrate the visual anomaly detection result maps of different methods on all six scenarios. In terms of visual effects, it is obvious that the proposed method has the best detection performance. As can be seen in Fig. 8, the noise suppression effect and the discrimination ability between the background and anomalies of the proposed method is good in S1 because the fractional transform is employed in the proposed method. As shown in the Figs. 9 and 12, the proposed method can detect more pixels in the detection results of S2 and R3. This phenomenon shows that the interference of the potential anomalies to the detection results is much reduced by adjusting the weight of each pixels in the saliency weighted matrix. In the detection result maps obtained by the LSD method and the proposed SSFSCRD method as shown in Figs. 9(i) and 10(i), it is clear that the spectral–spatial postprocessing procedure integrated in the proposed method can improve the detection capability more effectively.
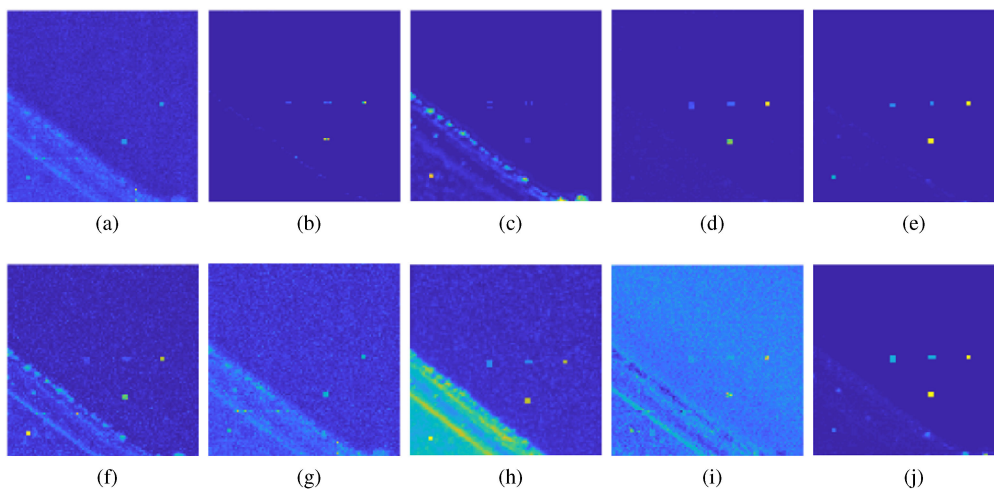
Fig. 8. The visual detection maps of the first synthetic dataset. (a) GRX method, (b) LRX method, (c) KRX method, (d) CRD method, (e) KCRD method, (f) PCA+RX method, (g) FrFE+RX method, (h) GTVLRR method, (i) LSD method, (j) SSFSCRD method.
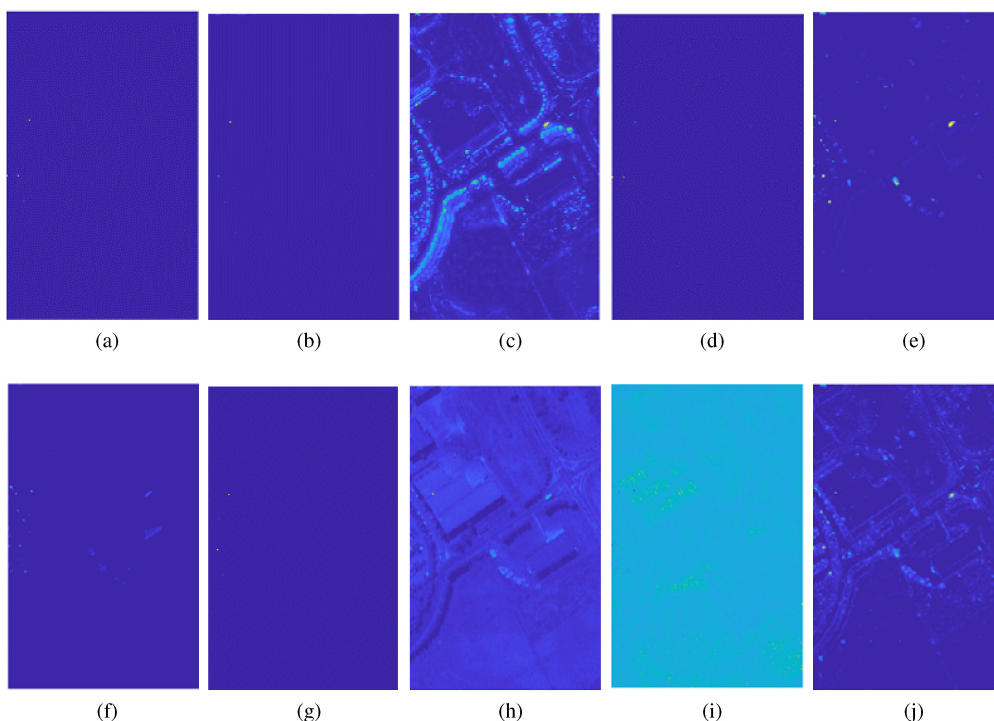

Fig. 9. The visual detection maps of the second synthetic dataset. (a) GRX method, (b) LRX method, (c) KRX method, (d) CRD method, (e) KCRD method, (f) PCA+RX method, (g) FrFE+RX method, (h) GTVLRR method, (i) LSD method, (j) SSFSCRD method.

Fig. 14 illustrates the ROC curves obtained for all methods with six HSI datasets. For S1 dataset shown in Fig. 14(a), it is clear that the proposed SSFSCRD method has better performance than all the other anomaly detection methods, as the FAR is about 0.08 when the TPR of the proposed SSFSCRD method climbs to 1. For the S2 dataset revealed in Fig. 14(b), the result of SSFSCRD demonstrates a better performance than other anomaly detection methods. When the TPR of the proposed SSFSCRD method is up to 1, the FAR is about 0.4. For the R1 dataset shown in Fig. 14(c), it is easy to find that the ROC curve of the proposed SSFSCRD method is always above those of other anomaly detection methods. For the R2 dataset shown in Fig. 14(d), the ROC curve of the proposed SSFSCRD method rises more sharply than the other anomaly detection methods. And when the TPR of the proposed SSFSCRD method is 1, the FAR of the proposed SSFSCRD method is approximately 0.1. For the R3 dataset, the ROC curve of the proposed SSFSCRD and LSD are almost the same and the results of ROC curve are consistent with the results of AUC value. As for the R4 dataset shown in Fig. 14(f), the ROC curve of the proposed SSFSCRD also increases relatively rapidly. And when the TPR of the proposed SSFSCRD is 1, the FAR of the proposed SSFSCRD
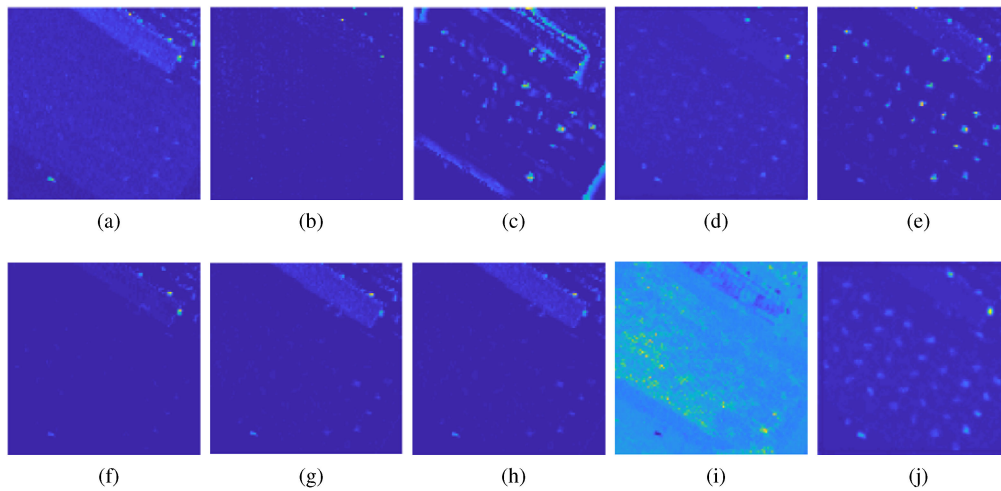
Fig. 10. Visual detection maps of the first real dataset. (a) GRX method. (b) LRX method. (c) KRX method. (d) CRD method. (e) KCRD method. (f) PCA+RX method. (g) FrFE+RX method. (h) GTVLRR method. (i) LSD method. (j) SSFSCRD method.
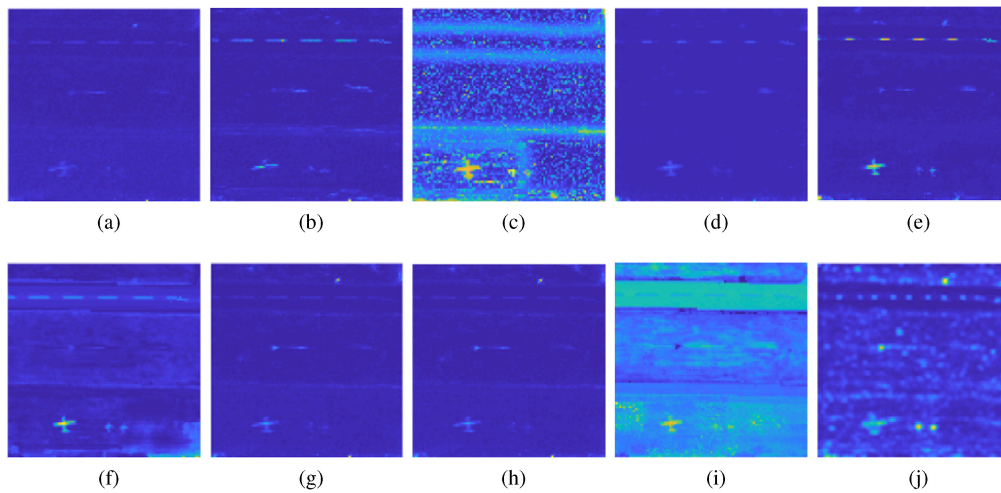

Fig. 11. Visual detection maps of the second real dataset. (a) GRX method. (b) LRX method. (c) KRX method. (d) CRD method. (e) KCRD method. (f) PCA+RX method. (g) FrFE+RX method. (h) GTVLRR method. (i) LSD method. (j) SSFSCRD method.
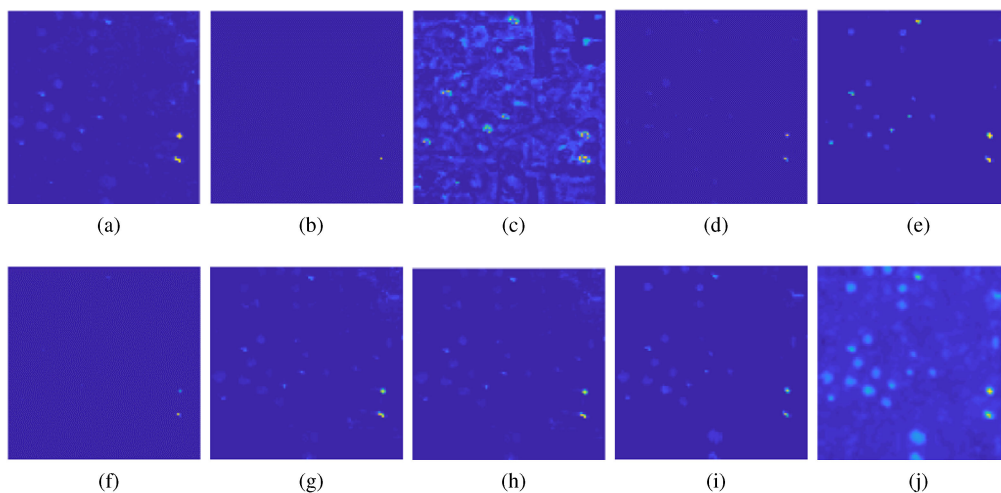

Fig. 12. Visual detection maps of the third real dataset. (a) GRX method. (b) LRX method. (c) KRX method. (d) CRD method. (e) KCRD method. (f) PCA+RX method. (g) FrFE+RX method. (h) GTVLRR method. (i) LSD method. (j) SSFSCRD method.
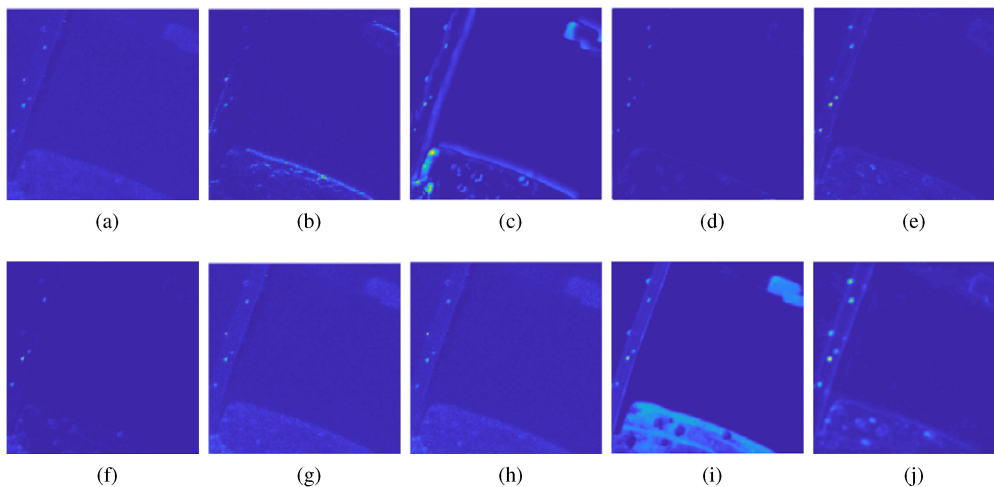
Fig. 13.   Visual detection maps of the fourth dataset. (a) GRX method. (b) LRX method. (c) KRX method. (d) CRD method. (e) KCRD method. (f) PCA+RX method. (g) FrFE+RX method. (h) GTVLRR method. (i) LSD method. (j) SSFSCRD method.
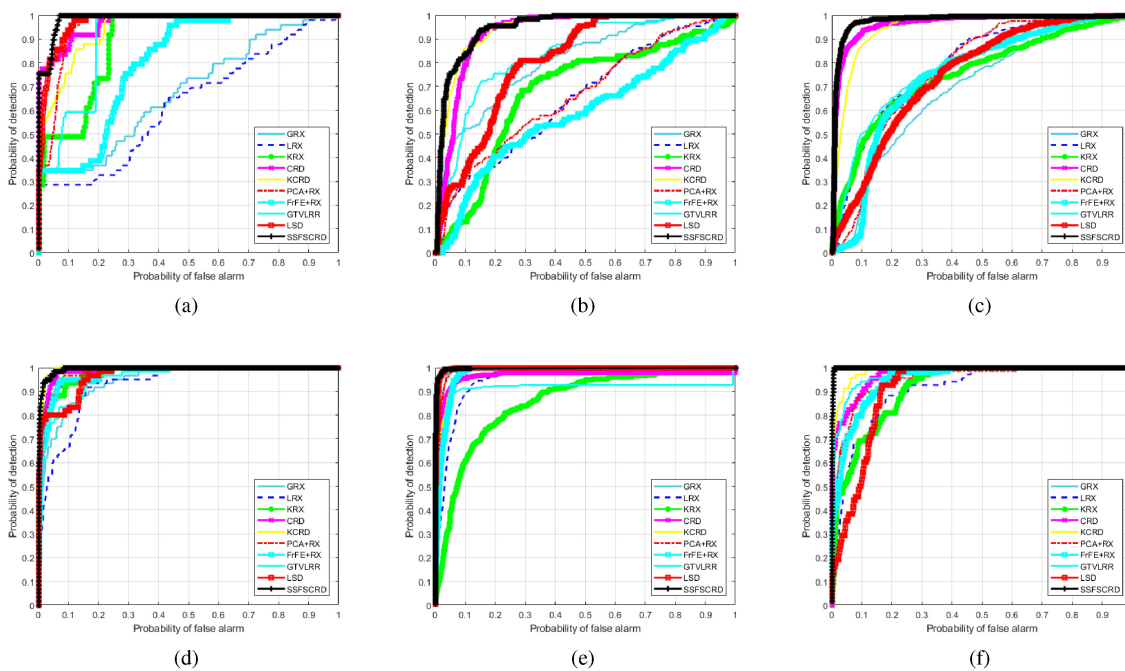

Fig. 14.   ROC curve of different anomaly detectors. (a) First synthetic dataset. (b) Second synthetic dataset. (c) First real dataset. (d) Second real dataset. (e) Third real dataset. (f) Fourth real dataset.

method is about 0.01. Above all, the ROC curves show that the detection probability of the proposed SSFSCRD method is higher than other compared methods at a lower FAR.

To demonstrate the separability between abnormal targets and background, we compare SSFSCRD with other methods by box graphs. As shown in Fig. 15, there are anomaly and background columns for each method, in which the detection values are normalized to 0–1. The red and green boxes in Fig. 15 represent the distribution of the abnormal targets' detection values and background's detection values, respectively. And their positions illustrate the separability of abnormal targets and background. Furthermore, the black line inside each box is the median values, and the upper and lower edges of the box reflect

10th and 90th percentiles, respectively. And the whiskers are the extreme values. For the S1 dataset shown in Fig. 15(a), the gaps between two abnormal targets and background for the proposed SSFSCRD method and GTVLRR method are bigger than the other methods. However, the upper whisker of background box for SSFSCRD method is lower than GTVLRR's, which means that the proposed SSFSCRD method suppresses the background more effectively than GTVLRR method. For the S2, R1, R3, and R4 datasets as shown in Fig. 15(b), (c), (e), and (f), it is obvious that the gaps between two abnormal targets and background for the proposed SSFSCRD method are bigger than other methods. For the R2 dataset, the gaps between abnormal targets and background for the proposed SSFSCRD method are nearly the
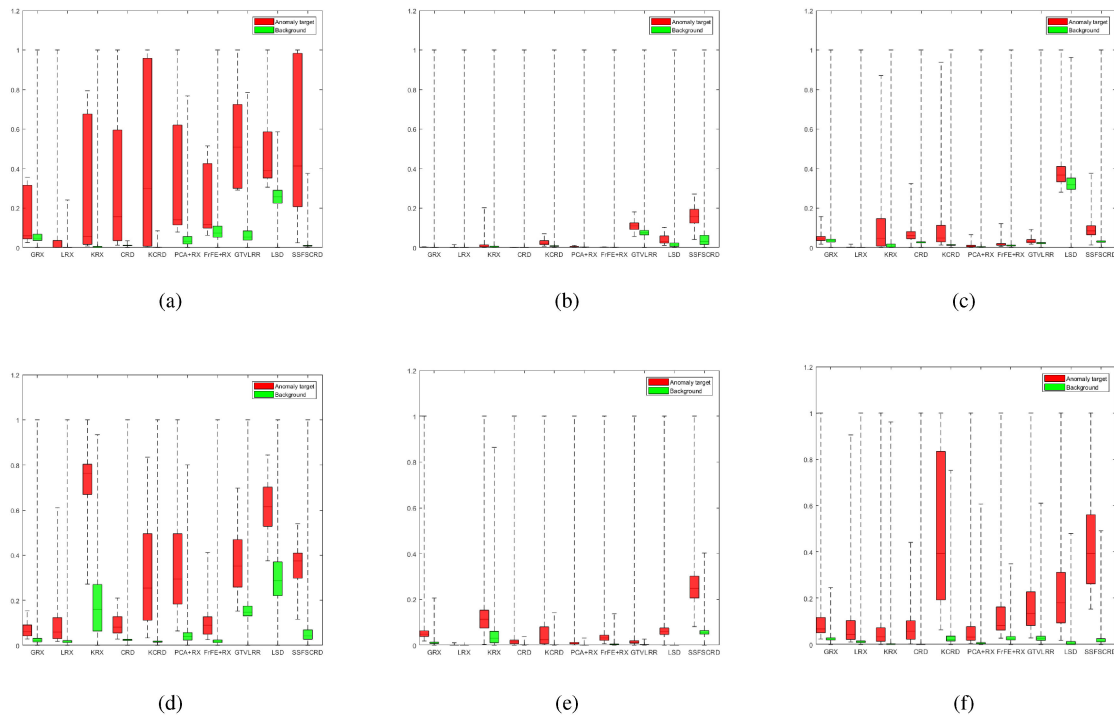
Fig. 15. Separability maps of different anomaly detectors. (a) First synthetic dataset. (b) Second synthetic dataset. (c) First real dataset. (d) Second real dataset. (e) Third real dataset. (f) Fourth real dataset.

same to those of the KRX method. Therefore, the results of separability maps of different methods reveal that the proposed SSFSCRD method has excellent discrimination ability between anomalies and background.

In summary, through comprehensive analysis of AUC values, visual detection results, ROC curves, and separability maps, the proposed SSFSCRD method is a significant and effective method compared with nine state-of-the-art HSI anomaly detection methods.

D. Capability of Suppressing Noise

By taking advantage of the suppressing noise ability of FrFT, Tao *et al.* employ FrFT as the preprocessing for RX detector [36]. To verify the capability of the proposed SSFSCRD method to suppress the noise, the relevant experiments are conducted in this section. We use the S1 dataset as the experimental dataset and add different levels of zero-mean Gaussian white noise into it. The SNR ranges from 20 to 60 dB and the step size is 10 dB. Table IV lists the AUC values of all detectors on the S1 dataset with different levels of zero-mean Gaussian white noise and the highest value under different levels of zero-mean Gaussian white noise is highlighted in italics. From Table IV, it can be seen that the proposed SSFSCRD always get the highest value under different levels of zero-mean Gaussian white noise. Besides, with the decreasing of SNR, the AUC values of SSFSCRD method drop to a small degree. Therefore, it can be concluded that the proposed SSFSCRD method can suppress the noise efficaciously.

TABLE IV
AUC VALUES OF ALL DETECTORS ON THE S1 DATASET WITH DIFFERENT
LEVELS OF ZERO-MEAN GAUSSIAN WHITE NOISE

Methods	SNR				
	20 dB	30 dB	40 dB	50 dB	60 dB
GRX	0.9029	0.9001	0.8951	0.8629	0.7349
LRX	0.9029	0.6949	0.6245	0.6199	0.6262
KRX	0.8991	0.8915	0.8911	0.8908	0.8910
CRD	0.9814	0.9832	0.9764	0.9751	0.9704
KCRD	0.9522	0.9496	0.9466	0.9477	0.9459
PCA+RX	0.9244	0.9468	0.9527	0.9540	0.9541
FrFE+RX	0.9057	0.9014	0.8899	0.8570	0.8118
GTVLRR	0.8025	0.8609	0.8124	0.7457	0.6461
LSD	0.9513	0.9717	0.9702	0.9733	0.9733
SSFSCRD	**0.9828**	**0.9860**	**0.9870**	**0.9874**	**0.9874**

Furthermore, Fig. 18 shows the comparison of the 50th band between the S1 data with 20 dB SNR and the FrFT domain of the S1 data with 20 dB SNR. It is clearly found that the FrFT can suppress the noise and make anomalies to be distinctive. In particular, the two targets in the bottom left corner cannot be distinguished under the interference of noise, but they can be clearly distinguished from the background after FrFT.

E. Computational Efficiency Analysis

The computational efficiency is also a significant criterion for evaluating the performance of HSI anomaly detector. For the proposed SSFSCRD method, the FrFT and the calculation of the weight vector α cost the most running time. Table V lists the running time of the SSFSCRD method and compared methods. It can be found that the running time of SSFSCRD is at a medium
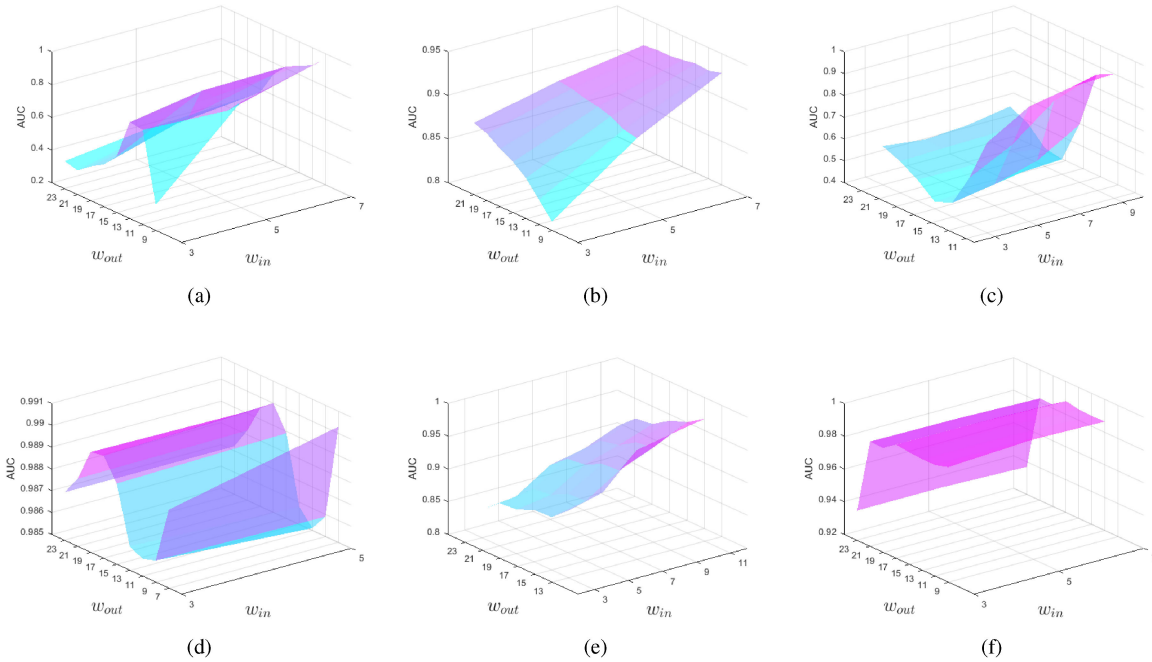
Fig. 16.   AUC values of the proposed method with respect to the outer window size w_{out} and the inner window size w_{in}. (a) First synthetic dataset. (b) Second synthetic dataset. (c) First real dataset. (d) Second real dataset. (e) Third real dataset. (f) Fourth real dataset.

TABLE V
RUNNING TIME (S) OF ALL DETECTORS ON SIX DATASETS

Methods	Running Time					
	S1	S2	R1	R2	R3	R4
GRX	0.5391	1.6872	0.6822	1.6323	1.9619	0.8696
LRX	11.8365	69.4491	15.5999	35.2566	44.9673	30.1980
KRX	21.9291	84.5402	25.0121	10.2365	42.4750	79.7452
CRD	5.5988	22.7656	5.5067	3.1692	7.5226	19.2305
KCRD	26.6035	110.6506	26.1087	12.946	39.4476	98.7999
PCA+RX	0.2036	1.2205	1.1195	0.2925	0.3417	0.4547
FrFE+RX	8.5641	50.0344	10.9230	12.7798	13.6224	19.4900
GTVLRR	187.1296	646.0585	104.7276	103.9034	108.5295	200.7451
LSD	3.7854	4.7501	5.7906	3.7791	1.3579	1.6794
SSFSCRD	7.7739	36.6782	7.4196	5.1295	11.8316	24.9713

level in the running time of all comparison algorithms. However, considering the excellent detection accuracy of SSFSCRD, the computational complexity of SSFSCRD is acceptable.

IV. DISCUSSION

The influence of crucial parameters involved in the proposed method are analyzed and discussed in this section. The proposed method contains four sensitive parameters in total. They are the window size, fractional order p, Lagrange multiplier λ, and the weighting coefficient β, respectively. The AUC value is adopted as evaluation standard to distinguish the effect of each parameter on the proposed method's performance. When analyzing one sensitive parameter, the values of other parameters are fixed as default parameters.

To analyze and discuss the effects of these parameters completely and objectively, explicit experiments are conducted on all the six HSI datasets. As for the window size parameters w_{in} and w_{out}, their effects are jointly analyzed. The fractional order p, Lagrange multiplier λ, and the weighting coefficient β are set

as 0.5, 0.5, and 10^{-6}, respectively. The experimental results are illustrated in Fig. 16.

Taking all the results of all the HSI datasets into consideration, the detection performance of the proposed method stably changes within a promising range in most cases. Specifically, for S2, R2, R3, and R4 dataset, when w_{out} is approximately less than 13, all the AUC values are good and nearly unchanged, which fully demonstrates the stability of the proposed method. As for S1 and R1 dataset, the AUC value changes a lot with w_{out} because the anomalies of these two datasets are close spatially. Furthermore, it is easy to find that the window size can affect the detection performance of the proposed method. A large outer window can provide sufficient background information, but potential anomalies and noise may also be used to represent the under test pixel. Therefore, the optimal window size may be different with different HSI datasets, and the optimal value of w_{in} should be a little larger than the size of anomalies.

For the fractional order p and the weighting coefficient β, their effects on the AUC value of the proposed method are given in Fig. 17. The fractional order p can reflect the amount of original spectral information contained in the FrFT domain. When the proposed method gets the best AUC value, the value of p is 0.8, 0.7, 0.3, 0.9, 0.3, and 0.3 on six HSI datasets, respectively. These results clearly demonstrate that taking advantage of the FrFT domain information can improve detection performance of the proposed method. As shown in Fig. 17(a) and (b), for the synthetic HSI datasets of S1 and S2, the optimal AUC values are 0.9856 and 0.9494 when β is 1. The anomalies in these two synthetic datasets are inserted artificially, and the sizes of these anomalies are very small. This situation does not meet the assumption that a pixel and its surrounding pixels in an HSI usually reflect the same or similar ground objects. However, for
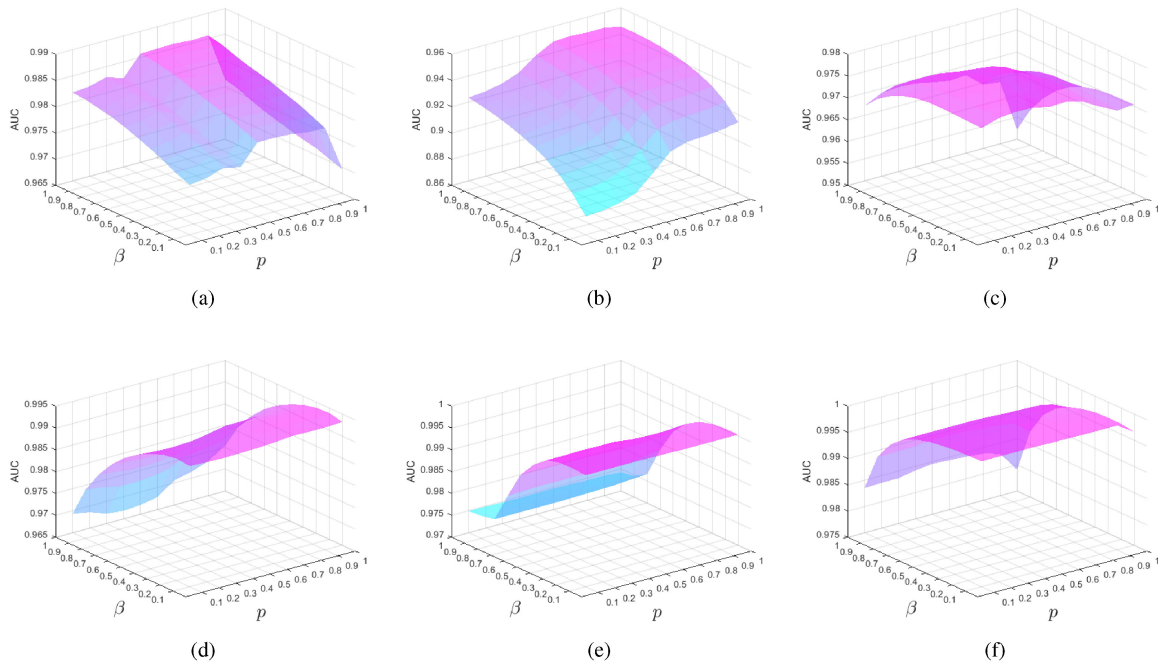
Fig. 17. AUC values of the proposed method with respect to the fractional order p and the weighting coefficient β. (a) First synthetic dataset. (b) Second synthetic dataset. (c) First real dataset. (d) Second real dataset. (e) Third real dataset. (f) Fourth real dataset.
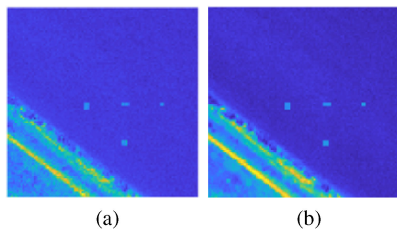

Fig. 18. Illustration with a hyperspectral band of the S1 dataset. (a) Fiftieth band of the data with 20 dB SNR. (b) Fiftieth band of the data with 20 dB SNR after FrFT when $p = 0.8$.

the real HSI datasets, the optimal AUC value is obtained when β is 0.1 or 0.2. Then, the AUC value rapidly decreases with the increase of β, and the smallest AUC value is obtained when β is 1. From the above analysis, for the real HSI datasets, it can be found that the best AUC values are reached when β is no larger than 0.5. This phenomenon shows that the proposed spectral–spatial postprocessing procedure is effective for improving the detection accuracy of hyperspectral anomaly detector.

V. CONCLUSION

This article proposes a spectral–spatial anomaly detection method based on FrFT and context-aware saliency-weighted collaborative representation for HSIs. The proposed method aims at solving the unsatisfactory detection performance caused by two problems. The first problem is that the background information is usually contaminated by the anomalies or noise, and the second one is the insufficient use of spatial information. The proposed method mainly consists of three important parts, including FrFT, context-aware saliency-weighted FrFTCRD,

and the spectral–spatial detection procedure. Through projecting all the hyperspectral pixels to the fractional Fourier domain, the noise can be suppressed and the anomalies can be highlighted. Referring to the relevant principles of context-aware saliency, a saliency-weighted matrix is designed as the regularization matrix. The new saliency-weighted regularization matrix uses both spectral and spatial information to set the weights for the background pixels, which can further reduce the influence of potential anomalies. Combining the new saliency-weighted regularization matrix with FrFT and CRD, a context-aware saliency-weighted FrFTCRD is designed to explore more accurate and pure background information. Consequently, collaborative represented background can not only have low noise influence, but also benefits from reducing effects of potential anomalies. To take advantage of the spatial information effectively, a spectral–spatial detection procedure is designed to calculate the final anomaly score for each PUT, which can further improve the performance of the proposed method. In order to evaluate the performance and effectiveness of the proposed methods, the proposed method is compared with nine state-of-the-art detectors on two synthetic HSI datasets and four real HSI datasets captured from different scenes. Extensive experimental results demonstrate that the proposed method outperforms other state-of-the-art anomaly detection methods on all six HSI datasets. Furthermore, through deeply analyzing and discussing the critical parameters, the proposed method also has good stability and effectiveness.

REFERENCES

[1] L. Ren, L. Zhao, and Y. Wang, "A superpixel-based dual window rx for hyperspectral anomaly detection," *IEEE Geosci. Remote Sens. Lett.*, vol. 17, no. 7, pp. 1233–1237, Jul. 2020.

[2] R. Zhao, Z. Shi, Z. Zou, and Z. Zhang, "Ensemble-based cascaded constrained energy minimization for hyperspectral target detection," *Remote Sens.*, vol. 11, p. 1310, May 2019.

[3] S. Li, K. Zhang, Q. Hao, P. Duan, and X. Kang, "Hyperspectral anomaly detection with multiscale attribute and edge-preserving filters," *IEEE Geosci. Remote Sens. Lett.*, vol. 15, no. 10, pp. 1605–1609, Oct. 2018.

[4] X. Yao and C. Zhao, "Hyperspectral anomaly detection based on the bilateral filter," *Infrared Phys. Techn.*, vol. 92, pp. 144–153, 2018.

[5] Y. Yang, J. Zhang, S. Song, C. Zhang, and D. Liu, "Low-rank and sparse matrix decomposition with orthogonal subspace projection-based background suppression for hyperspectral anomaly detection," *IEEE Geosci. Remote Sens. Lett.*, vol. 17, no. 8, pp. 1378–1382, Aug. 2020.

[6] S. Chang, B. Du, and L. Zhang, "BASO: A background-anomaly component projection and separation optimized filter for anomaly detection in hyperspectral images," *IEEE Trans. Geosci. Remote Sens.*, vol. 56, no. 7, pp. 3747–3761, Jul. 2018.

[7] L. Zhu, G. Wen, S. Qiu, and X. Zhang, "Improving hyperspectral anomaly detection with a simple weighting strategy," *IEEE Geosci. Remote Sens. Lett.*, vol. 16, no. 1, pp. 95–99, Jan. 2019.

[8] Z. Li and Y. Zhang, "A new hyperspectral anomaly detection method based on higher order statistics and adaptive cosine estimator," *IEEE Geosci. Remote Sens. Lett.*, vol. 17, no. 4, pp. 661–665, Apr. 2020.

[9] I. S. Reed and X. Yu, "Adaptive multiple-band CFAR detection of an optical pattern with unknown spectral distribution," *IEEE Trans. Acoust. Speech Signal Process*, vol. 38, no. 10, pp. 1760–1770, Oct. 1990.

[10] W. Xie, B. Liu, Y. Li, J. Lei, C. Chang, and G. He, "Spectral adversarial feature learning for anomaly detection in hyperspectral imagery," *IEEE Trans. Geosci. Remote Sens.*, vol. 58, no. 4, pp. 2352–2365, Apr. 2020.

[11] X. Zhang, G. Wen, and W. Dai, "A tensor decomposition-based anomaly detection algorithm for hyperspectral image," *IEEE Trans. Geosci. Remote Sens.*, vol. 54, no. 10, pp. 5801–5820, Oct. 2016.

[12] W. Zhang, X. Lu, and X. Li, "Similarity constrained convex nonnegative matrix factorization for hyperspectral anomaly detection," *IEEE Trans. Geosci. Remote Sens.*, vol. 57, no. 7, pp. 4810–4822, Jul. 2019.

[13] Y. Xu, Z. Wu, J. Li, A. Plaza, and Z. Wei, "Anomaly detection in hyperspectral images based on low-rank and sparse representation," *IEEE Trans. Geosci. Remote Sens.*, vol. 54, no. 4, pp. 1990–2000, Apr. 2016.

[14] Y. Zhang, D. Bo, L. Zhang, and S. Wang, "A low-rank and sparse matrix decomposition-based Mahalanobis distance method for hyperspectral anomaly detection," *IEEE Trans. Geosci. Remote Sens.*, vol. 54, no. 3, pp. 1376–1389, Mar. 2016.

[15] Q. Guo, B. Zhang, Q. Ran, L. Gao, J. Li, and A. Plaza, "Weighted-RXD and linear filter-based RXD: Improving background statistics estimation for anomaly detection in hyperspectral imagery," *IEEE J. Sel. Topics Appl. Earth Observ. Remote Sens.*, vol. 7, no. 6, pp. 2351–2366, Jun. 2014.

[16] N. Billor, A. S. Hadi, and P. F. Velleman, "BACON: Blocked adaptive computationally efficient outlier nominators," *Comput. Stat. Data Anal.*, vol. 34, no. 3, pp. 279–298, 2000.

[17] Y. Xu, B. Du, L. Zhang, and S. Chang, "A low-rank and sparse matrix decomposition-based dictionary reconstruction and anomaly extraction framework for hyperspectral anomaly detection," *IEEE Geosci. Remote Sens. Lett.*, vol. 17, no. 7, pp. 1248–1252, Jul. 2020.

[18] H. Kwon and N. Nasrabadi, "Kernel RX-algorithm: A nonlinear anomaly detector for hyperspectral imagery," *IEEE Trans. Geosci. Remote Sens.*, vol. 43, no. 2, pp. 388–397, Feb. 2005.

[19] S. Khazai and B. Mojaradi, "A modified kernel-RX algorithm for anomaly detection in hyperspectral images," *Arab. J. Geosci.*, vol. 8, no. 3, pp. 1487–1495, 2013.

[20] B. Du and L. Zhang, "Random-selection-based anomaly detector for hyperspectral imagery," *IEEE Trans. Geosci. Remote Sens.*, vol. 49, no. 5, pp. 1578–1589, May 2011.

[21] M. J. Carlotto, "A cluster-based approach for detecting man-made objects and changes in imagery," *IEEE Trans. Geosci. Remote Sens.*, vol. 43, no. 2, pp. 374–387, Feb. 2005.

[22] C. Zhao and L. Zhang, "Spectral-spatial stacked autoencoders based on low-rank and sparse matrix decomposition for hyperspectral anomaly detection," *Infrared Phys. Techn.*, vol. 92, pp. 166–176, 2018.

[23] D. Ma, Y. Yuan, and Q. Wang, "Hyperspectral anomaly detection based on separability-aware sample cascade," *Remote Sens.*, vol. 11, no. 21, p. 2537, 2019.

[24] Y. Chen, N. M. Nasrabadi, and T. D. Tran, "Simultaneous joint sparsity model for target detection in hyperspectral imagery," *IEEE Geosci. Remote Sens. Lett.*, vol. 8, no. 4, pp. 676–680, Jul. 2011.

[25] Y. Zhang, B. Du, L. Zhang, and S. Wang, "A low-rank and sparse matrix decomposition-based Mahalanobis distance method for hyperspectral anomaly detection," *IEEE Trans. Geosci. Remote Sens.*, vol. 54, no. 3, pp. 1376–1389, Mar. 2016.

[26] R. Zhao, B. Du, and L. Zhang, "Hyperspectral anomaly detection via a sparsity score estimation framework," *IEEE Trans. Geosci. Remote Sens.*, vol. 55, no. 6, pp. 3208–3222, Jun. 2017.

[27] T. Cheng and B. Wang, "Graph and total variation regularized low-rank representation for hyperspectral anomaly detection," *IEEE Trans. Geosci. Remote Sens.*, vol. 58, no. 1, pp. 391–406, Jan. 2020.

[28] W. Li and Q. Du, "Collaborative representation for hyperspectral anomaly detection," *IEEE Trans. Geosci. Remote Sens.*, vol. 53, no. 3, pp. 1463–1474, Mar. 2015.

[29] H. Su, Z. Wu, Q. Du, and P. Du, "Hyperspectral anomaly detection using collaborative representation with outlier removal," *IEEE J. Sel. Topics Appl. Earth Observ. Remote Sens.*, vol. 11, no. 12, pp. 5029–5038, Dec. 2018.

[30] P. Gurram, H. Kwon, Z. Peng, and W. Yin, "Sparse kernel learning-based feature selection for anomaly detection," *IEEE Trans. Aerosp. Electron. Syst.*, vol. 51, no. 3, pp. 1698–1716, Jul. 2015.

[31] S. Valero, P. Salembier, and J. Chanussot, "Hyperspectral image representation and processing with binary partition trees," *IEEE Trans. Image Process.*, vol. 22, no. 4, pp. 1430–1443, Apr. 2013.

[32] A. Plaza *et al.*, "Recent advances in techniques for hyperspectral image processing," *Remote Sens. Environ.*, vol. 113, pp. S110–S122, 2009.

[33] Z. Yuan, H. Sun, K. Ji, Z. Li, and H. Zou, "Local sparsity divergence for hyperspectral anomaly detection," *IEEE Geosci. Remote Sens. Lett.*, vol. 11, no. 10, pp. 1697–1701, Oct. 2014.

[34] B. Tu, N. Li, Z. Liao, X. Ou, and G. Zhang, "Hyperspectral anomaly detection via spatial density background purification," *Remote Sens.*, vol. 11, no. 22, p. 2618, 2019.

[35] K. Tan, Z. Hou, D. Ma, Y. Chen, and Q. Du, "Anomaly detection in hyperspectral imagery based on low-rank representation incorporating a spatial constraint," *Remote Sens.*, vol. 11, no. 13, p. 1578, 2019.

[36] R. Tao, X. Zhao, W. Li, H. Li, and Q. Du, "Hyperspectral anomaly detection by fractional fourier entropy," *IEEE J. Sel. Topics Appl. Earth Observ. Remote Sens.*, vol. 12, no. 12, pp. 4920–4929, Dec. 2019.

[37] V. A. Narayanan and K. M. M. Prabhu, "The fractional Fourier transform: Theory, implementation and error analysis," *Microprocess. Microsyst.*, vol. 27, no. 10, pp. 511–521, 2003.

[38] S. Huang, S. Fang, and N. Han, "Parameter estimation of delay-doppler underwater acoustic multi-path channel based on iterative fractional fourier transform," *IEEE Access*, vol. 7, pp. 7920–7931, 2019.

[39] S. Goferman, L. Zelnik-Manor, and A. Tal, "Context-aware saliency detection," *IEEE Trans. Pattern Anal. Mach. Intell.*, vol. 34, no. 10, pp. 1915–1926, Oct. 2012.

[40] X. Luo, J. Zhang, and Q. Dai, "Saliency-based geometry measurement for image fusion performance," *IEEE Trans. Instrum. Meas.*, vol. 61, no. 4, pp. 1130–1132, Apr. 2012.

[41] W. Liu *et al.*, "Random selection-based adaptive saliency-weighted RXD anomaly detection for hyperspectral imagery," *Int. J. Remote Sens.*, vol. 39, no. 8, pp. 2139–2158, 2018.

[42] H. Zhang, H. Zhai, L. Zhang, and P. Li, "Spectral–spatial sparse subspace clustering for hyperspectral remote sensing images," *IEEE Trans. Geosci. Remote Sens.*, vol. 54, no. 6, pp. 3672–3684, Jun. 2016.

[43] L. Zhang and C. Zhao, "A spectral-spatial method based on low-rank and sparse matrix decomposition for hyperspectral anomaly detection," *Int. J. Remote Sens.*, vol. 38, no. 14, pp. 4047–4068, 2017.

[44] C. Zhao, L. Zhang, and B. Cheng, "A local Mahalanobis-distance method based on tensor decomposition for hyperspectral anomaly detection," *Geocarto Int.*, vol. 34, no. 5, pp. 490–503, 2019.

[45] K. Tan, Z. Hou, D. Ma, Y. Chen, and Q. Du, "Anomaly detection in hyperspectral imagery based on low-rank representation incorporating a spatial constraint," *Remote Sens.*, vol. 11, p. 1578, Jul. 2019.

[46] W. Xie, B. Liu, Y. Li, J. Lei, C. Chang, and G. He, "Spectral adversarial feature learning for anomaly detection in hyperspectral imagery," *IEEE Trans. Geosci. Remote Sens.*, vol. 58, no. 4, pp. 2352–2365, Apr. 2020.

[47] Y. Yang, S. Song, D. Liu, J. C.-W. Chan, J. Li, and J. Zhang, "Hyperspectral anomaly detection through sparse representation with tensor decomposition-based dictionary construction and adaptive weighting," *IEEE Access*, vol. 8, pp. 72121–72137, 2020.

[48] J. Lei, W. Xie, J. Yang, Y. Li, and C. Chang, "Spectral–spatial feature extraction for hyperspectral anomaly detection," *IEEE Trans. Geosci. Remote Sens.*, vol. 57, no. 10, pp. 8131–8143, Oct. 2019.

[49] X. Kang, X. Zhang, S. Li, K. Li, J. Li, and J. A. Benediktsson, "Hyperspectral anomaly detection with attribute and edge-preserving filters," *IEEE Trans. Geosci. Remote Sens.*, vol. 55, no. 10, pp. 5600–5611, Oct. 2017.

[50] S. Li, K. Zhang, P. Duan, and X. Kang, "Hyperspectral anomaly detection with kernel isolation forest," *IEEE Trans. Geosci. Remote Sens.*, vol. 58, no. 1, pp. 319–329, Jan. 2020.

[51] P. Xiang, J. Song, H. Li, L. Gu, and H. Zhou, "Hyperspectral anomaly detection with harmonic analysis and low-rank decomposition," *Remote Sens.*, vol. 11, no. 24, p. 3028, 2019.

[52] R. Li and S. Latifi, "Improving hyperspectral subpixel target detection using hybrid detection space," *J. Appl. Remote Sens.*, vol. 12, no. 1, p. 015022, 2018.

[53] N. Ma, X. Yu, Y. Peng, and S. Wang, "A lightweight hyperspectral image anomaly detector for real-time mission," *Remote Sens.*, vol. 11, no. 13, p. 1622, 2019.

Chunhui Zhao received the B.S. and M.S. degrees from Harbin Engineering University, China, in 1986 and 1989, respectively, and the Ph.D. degree from the Department of Automatic Measure and Control, Harbin Institute of Technology, China, in 1998, all in information and communication engineering.

He was a Postdoctoral Research Fellow with the College of Underwater Acoustical Engineering, Harbin Engineering University. At present, he is a Professor and Doctoral Supervisor with the College of Information and Communication Engineering, Harbin Engineering University.

His research interests include digital signal and image processing, mathematical morphology, and hyperspectral remote sensing image processing.

Dr. Zhao is a senior member of Chinese Electronics Academy.

Chuang Li (Graduate Student Member, IEEE) is working toward the Ph.D. degree in information and communication engineering at the Harbin Engineering University, China. His research interests include hyperspectral image processing, etc.

Shou Feng received the Ph.D. degree in information and communication engineering from the Harbin Institute of Technology, China, in 2019.

He is an Assistant Professor with Harbin Engineering University, China. His research interests include remote sensing image processing, data mining, machine learning, etc.
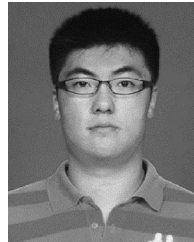
Nan Su received the Ph.D. degree in information and communication engineering from the Harbin Institute of Technology, China, in 2017.

He is an Associate Professor with the Harbin Engineering University, China. His research interests include remote sensing image processing, data mining, etc.

Wei Li (Senior Member, IEEE) received the B.E. degree in telecommunications engineering from Xidian University, Xian, China, in 2007, the M.S. degree in information science and technology from Sun Yat-Sen University, Guangzhou, China, in 2009, and the Ph.D. degree in electrical and computer engineering from Mississippi State University, Starkville, MS, USA, in 2012.

He spent one year as a Postdoctoral Researcher with the University of California, Davis, CA, USA. He is currently a Professor with the School of Information and Electronics, Beijing Institute of Technology, Beijing, China. His research interests include hyperspectral image analysis, pattern recognition, and data compression.